Morphological changes under strain for different thermoplastic polyurethanes monitored by SAXS related to strain-at-break

Almut Stribeck[1*], Xuke Li[1], Ahmad Zeinolebadi[2], Elmar Pöselt[3], Berend Eling[3], Sérgio Funari[4]

[1]University of Hamburg, Department of Chemistry, Institute TMC, Bundesstr. 45, 20146 Hamburg, Germany

[2]Polymer Consult Buchner GmbH, Schwarzer Weg 34, 22309 Hamburg, Germany

[3]BASF Polyurethanes GmbH, Elastogranstr. 60, 49448 Lemförde, Germany

[4]HASYLAB at DESY, Notkestr. 85, 22603 Hamburg, Germany

[*]E-mail: almut@stribeck.de

Abstract. In tensile tests of 6 different hand-cast thermoplastic polyurethanes (TPU) with a hard-segment content HSC=0.51 the volume fraction of hard domains (VH) has been tracked. The materials exhibit a linear increase up to a strain of approx. 0.5 (strain-induced phase separation). Thereafter a linear decrease of VH is indicated. When stretched by 100% about 25% of the initially present hard domains are destroyed. The extrapolation to VH=0 is close to the elongation at break. Characteristic materials parameters are suggested by the found relation.

The tests (maximum strain: 3) are monitored by small-angle X-ray scattering (SAXS). The morphology is closer to particle scattering than that of machine-processed material. Therefore the longitudinal scattering appears fittable by a one-dimensional statistical model that separates the weak discrete scattering from the height distribution of hard domains, whose weight returns the variation of VH with the strain. All TPUs are based on 4,4'-methylene diphenyl diisocyanate (MDI). The other raw components are systematically varied.

Two MDI units determine the height of the average hard domain. The variation of VH with strain is described by a tensile augmentation (in analogy to the tensile strength) which is realized at an end-of-growth strain. The following hard domain destruction is governed by a consumption factor. Deviations between extrapolated and measured strain at break may be related to the TPU composition.

1 Introduction

Thermoplastic polyurethanes (TPU) are produced in the reaction of a diisocyanate, a short-chain diol and a polyol. The isocyanate and short-chain diol form a rigid or hard segment; these isocyanate-ended hard segments are linked through the polyol soft block to form a statistical block copolymer of the $(A-B)_n$ type. When all the components of the polyurethane are difunctional, a linear thermoplastic polymer is obtained. As the hard and soft chain segments are thermodynamically incompatible, phase separation occurs resulting in the formation of domains that are either rich in soft or hard segments. The exact nature of the final morphology depends on both the molecular composition and the processing conditions. As far as the molecular composition is concerned, it is commonly accepted that the extent to which phase separation in the elastomer takes place depends on: i) the distribution of hard and soft chain segments along the chain, ii) the polarity difference or the compatibility between hard and soft chain segments and iii) the ability of the hard-segments to stack tightly and to establish strong intra-molecular interactions. Another generalization concerning phase separation may be that the larger the difference between the glass transition temperatures of the soft and hard segment rich domains is, the higher is the extent of phase segregation between the phases. This fact also reflects differences in polarity between the hard and soft chain segments.[1]

When TPUs are synthesized in a one-shot method, the raw components are simply stirred together. On a large scale, the process is carried out by machines (machine processing). "Hand-casting" refers to a process in which the components are poured into a bucket[2] and stirred. In such a "bucket and paddle mix",[3] the mixing quality may remain moderate. In other words, at different places in the bucket copolymer chains with different sequence statistics will have grown. The mixture is poured onto a cool plate for curing. During this step the formation of convection cells is observed. Material taken from the center of the convection cells exhibits different composition as compared to material from the edges of the convection cells.[4] So in the block sequences of hand cast material a double variability is found, where the primary one is the result of the statistical nature of the polyaddition. This will probably affect even the morphology of hard and soft domains, which should exhibit greater variability of domain sizes. Ultimately, hand-casting might even have an impact on the materials properties. In studies that vary the molding conditions, effects on the materials performance have been reported for PU[5–7] or epoxy resin.[8]

In this study we carry out straining experiments and simultaneously monitor the evolution of its morphology by small-angle X-ray scattering (SAXS). To quantify the aforementioned extra disorder in the already irregular topology of PU is difficult even if scattering methods are employed. Here it may help to project the scattering data back into real space using procedures similar to those used in computed tomography. In a parallel study[9] of machine-processed thermoplastic polyurethane (TPU) we have described morphological peculiarities that have become visible after such a transformation. They have been related to excellent homogeneity of the mixing[3] in the machine process and the addressed primary variability of block sequence. Now we investigate corresponding hand-cast material.

Compared to machine-processed TPU the morphology of hand-cast material resembles an ensemble of particles which are almost uncorrelated. In this study we propose a procedure to strip the small effect of correlations from the scattering data by fitting, and thus to

extract information on the ensemble of the uncorrelated particles.[10] As a function of strain one expects that the hard domains appear rigid, and that the gaps formed by the soft domains expand with strain. As this feasibility test is passed we determine the variation of hard-domain volume in the strain test and find a relation to one of the ultimate properties[5,11] of the materials. To the best of our knowledge neither the variation of the hard domain content during straining nor its relation to the strain at break has been quantified before.

2 Experimental

2.1 Materials

We study thermoplastic polyurethanes (TPU) made from different components. The hard segments of all materials are made from 4,4'-methylene diphenyl diisocyanate (MDI). The chain extenders are 1,4-butane diol (BD) or hydroquinone bis(2-hydroxyethyl) ether (HQEE), respectively. The soft segments are either made from polytetrahydrofuran (PTHF®, PTHF is a trade mark of BASF SE), from polycaprolactone (PCL) or from adipic ester (AE). The molar masses of all soft segments are very close to $M_n \approx 1000$ Da.

The raw materials have been produced by BASF and all TPUs have been synthesized by BASF Polyurethanes Ltd in Lemförde, Germany by hand-casting in a one-shot process.[12] After curing the materials have been milled and injection molded to sheets of 2 mm thickness. Afterwards they have been matured[13–19] by annealing at 100 °C for 20 h.

Table 1 presents characterizations of the materials. σ_{max} and ε_b have been determined in separate tensile tests. The reported values for ε_b are the maximum values from several repeated determinations. The hard segment content is calculated according to

$$\mathrm{HSC} = \frac{\mathrm{n}_{chain\,extender}\left(\mathrm{M}_{chain\,extender} + \mathrm{M}_{diisocyanate}\right)}{\mathrm{m}_{total}}$$

whilst neglecting the second terminal diisocyanate.

Wide-angle X-ray scattering (WAXS) scans of the isotropic materials have been carried out in a powder diffractometer X'Pert Pro MPD manufactured by PANalytical in Bragg-Brentano geometry with a wavelength $\lambda = 0.1542$ nm (Cu-k$_\alpha$). The scans cover the angular range $2° \leq 2\theta \leq 42°$. 2θ is the scattering angle.

2.2 Tensile testing

Tests are run in a self-made[20] machine. A grid of fiducial marks is printed[21] on test bars S3 (DIN 50125). The sample thickness is $t_{s0} \approx 2$ mm. The sample width is 2 mm. The clamping length is 22.5 mm. Signals from the transducer are recorded during the experiment. The sample is monitored by a TV-camera. Video frames are grabbed every 12 s and are stored together with the experimental data. The machine is operated at a cross-head speed of 1 mm/min. Using the fiducial marks, the local macroscopic strain $\varepsilon = (\ell - \ell_0)/\ell_0$ at the position of X-radiation is computed automatically from the initial distance, ℓ_0, between two fiducial marks and the respective actual distance, ℓ. Processing all the video frames yields the curve $\varepsilon(t)$ as a function of the elapsed time. It is very well approximated by a quadratic polynomial. The local strain rate is kept low $\dot{\varepsilon} \approx 1.3 \times 10^{-3}\,\mathrm{s}^{-1}$ in order to adapt to the limitations of the synchrotron beamline. The true stress, $\sigma = F/A$, is computed from the force F measured by the load cell after subtracting the force exerted by the upper sample clamp, and from $A = A_0/(1+\varepsilon)$, the estimated actual sample cross-section. A_0 is the initial cross section of the central zone of the test bar.

Table 1: Samples and their characterization. ρ: mass density, σ_{max}: tensile strength, ε_b: elongation at break, $M_{w,TPU}$: weight-average molecular mass of the polymer, $X_{iso,TPU}$: isocyanate content of the polymer. All materials share the same hard-segment content HSC=51%.

labeling	mbt	mqt	mbl	mql	mba	mqa
hard segment	MDI	MDI	MDI	MDI	MDI	MDI
chain extender	BD	HQEE	BD	HQEE	BD	HQEE
soft segment	PTHF	PTHF	PCL	PCL	AE	AE
ρ [g/cm]	1.172	1.185	1.215	1.23	1.239	1.255
Shore D	65	64	71	75	71	74
σ_{max} [MPa]	54	40	42	33	42	34
ε_b	5.0	4.6	4.9	3.9	5.6	4.7
$M_{w,TPU}$ [kDa]	88	55	103	54	80	66
$X_{iso,TPU}$ [%]	0.06	0.10	0.04	0.04	0.04	0.08

The experiments are stopped at $\varepsilon \approx 3$ when the observed SAXS intensity has become too low for a quantitative analysis.

2.3 SAXS monitoring

SAXS is carried out in the synchrotron beamline A2 at HASYLAB, Hamburg, Germany. The wavelength of radiation is $\lambda = 0.15$ nm, and the sample-detector distance is 3022 mm. Scattering patterns are collected by a 2D marccd 165 detector (mar research, Norderstedt, Germany) in binned 1024 $\times$ 1024 pixel mode (pixel size: 158.2 µm $\times$ 158.2 µm). Scattering patterns are recorded every 132 s with an exposure of 120 s. The patterns $I(\mathbf{s}) = I(s_{12}, s_3)$ cover the region $-0.21\,\mathrm{nm}^{-1} \leq s_{12}, s_3 \leq 0.21\,\mathrm{nm}^{-1}$. $\mathbf{s} = (s_{12}, s_3)$ is the scattering vector with its modulus defined by $|\mathbf{s}| = s = (2/\lambda)\sin\theta$. It is not necessary to emphasize the small amount of extrapolated data at the beamstop, because it covers an angular region in which the correlation among the hard domains has already dropped to zero. The scattering patterns are normalized and background corrected.[22] This means intensity normalization for constant primary beam flux, zero absorption, and constant irradiated volume V_0. Because the samples are narrower than the primary beam, the latter correction has been carried out by $V(t)/V_0 = 1/(1+\varepsilon(t))$. The equation assumes constant sample volume and a sample that is fully immersed in the X-ray beam. Absorption factors $\exp(-\mu t_{s0})$ of the unstrained samples are determined by measuring the primary beam flux in front of the detector with and without a sample, respectively. From the result the linear absorption factor, μ, is computed using the known sample thickness. Finally the actual absorption factor $\exp(-\mu t_s(t))$ that compensates the lateral thinning as well is assessed using $t_s(t) = t_{s0}/(1+\varepsilon(t))$. The absorption correction is carried out by dividing the pattern intensity by $t_s(t)$ followed by the subtraction of the machine background. The strain that is associated to each scattering pattern is related to the time $t + t_e/2$ with t being the elapsed time at the start of the exposure, and t_e the total exposure of the pattern. After these steps the resulting scattering patterns are still not in absolute units, but their intensities can be compared relatively to each other. This pre-evaluation is carried out automatically by procedures written in PV-WAVE.[23]

2.4 SAXS data analysis

Analysis of projections. The best-known projection in the field of scattering maps the intensity $I(\mathbf{s})/V$ that is normalized to the irradiated volume, V, onto the zero–dimensional subspace. The resulting number Q is known as "invariant" or "scattering power"

$$\{I\}_0/V = Q = \int I(\mathbf{s})/V\, d^3s.$$

In a two-phase system $Q = v_h(1-v_h)(\rho_h-\rho_s)^2$ is valid with v_h the volume fraction of hard domains, ρ_h and ρ_s being the electron densities of the hard domain phase and the soft phase, respectively.

Bonart's longitudinal scattering[24] is obtained by not integrating over the whole reciprocal space, but only over planes normal to the fiber axis yielding the curve

$$\{I\}_1(s_3)/V = 2\pi \int_0^\infty s_{12} I(s_{12}, s_3)/V\, ds_{12},$$

which is a function of the straining direction s_3. $\{I\}_1(s_3)$ is a projection onto a 1D subspace as indicated by subscripting to the pair of braces. Projections are computed from normalized patterns.

From such projections interface distribution functions[22,25,26] (IDF) $g_1(r_3)$ are computed for further analysis. In this way it becomes possible to quantify several morphological parameters.

Technically, the first step involves subtraction of a guessed constant density fluctuation background,[27–29] I_{Fl}, from the measured curve and multiplication by $4\pi^2 s_3^2$ to apply the second derivative in reciprocal space. The result is an intermediate interference function

$$G_{1,i}(s_3) = (\{I\}_1(s_3)/V - I_{Fl})\, 4\pi^2 s_3^2.$$

The final background is constructed by application of a narrow low-pass frequency filter to $G_{1,i}(s_3)$, as is described elsewhere.[22,30] Thus the interference function $G_1(s_3)$ is obtained. Its one-dimensional Fourier transform is the longitudinal IDF $g_1(r_3)$.

The IDF is fitted[26] by a one-dimensional model that describes the arrangement of alternating hard-domain heights and soft-domain heights along the straining direction. Visual inspection of the computed IDFs shows that the height distributions of hard domains can be modeled by Gaussian functions and that the range of correlation among the domains is short. Thus a short-range stacking model[26] with few parameters is chosen, which is a variant of the ideal stacking model.[31] The parameters of the model are a weight W that is related to the volume fraction of contributing chords (cf. Figure 1), average heights $\bar{H}_h$ and $\bar{H}_s$ of hard and soft domains, respectively, and the relative standard deviations $\sigma_h/\bar{H}_h$ and $\sigma_s/\bar{H}_s$ of the domain height distributions. An additional parameter that skews[32,33] the Gaussians is present but not discussed here.

Fitted parameters and hard domain volume. By fitting the IDF, we determine the height distributions $H_h(r_3)$ and $H_s(r_3)$ of hard and soft domain chords, respectively. The weight parameter of the IDF is defined

$$W = \int H_h(r_3)\, dr = \int H_s(r_3)\, dr. \quad (1)$$

Let us assume that the hard domains are the diluted phase, i.e. that the small-angle scattering counts all the chords which cross all the hard domains (in the matrix phase there may be chords which are so long that they will not be counted). Without loss of generality we consider a single hard domain. Figure 1 shows a sketch of this hard domain intersected by its chords. Obviously, the volume V_h of the hard domain is

$$V_h = d\sigma \iint l(r_1, r_2)\, dr_1 dr_2 = d\sigma \int r_3 H_h(r_3)\, dr_3, \quad (2)$$

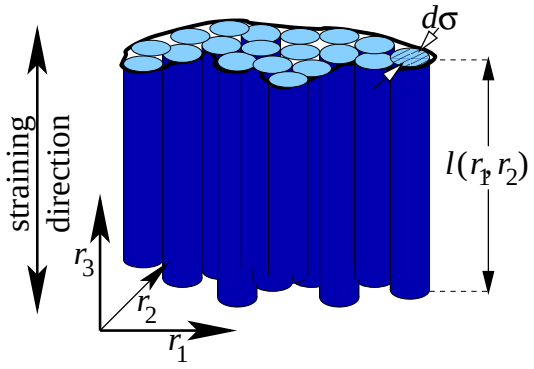

Figure 1: The (only) hard domain of a primitive morphology intersected by chords of varying length l, the lengths defined by the surface of the hard domain. Every chord occupies an infinitesimal cross section $d\sigma$. Only chords which run in straining direction are considered, because the longitudinal scattering $\{I\}_1(r_3)$ is analyzed

and the change of the integration variables from the first to the second integral is possible, because $H_h(r_3)$ is just the function which gives the number of chords of length r_3. Moreover, the average hard-domain height is defined as usual

$$\overline{H}_h = \frac{\int r_3 H_h(r_3)\, dr_3}{\int H(r_3)\, dr_3} = \frac{V_h/d\sigma}{W}, \qquad (3)$$

and it follows

$$\overline{H}_h W \propto V_h. \qquad (4)$$

Both $\overline{H}_h$ and W are fit parameters. Thus a quantity which is proportional to the total volume of hard domains can be determined from the fit. In the special case of rigid hard domains the proportionality even simplifies to $W \propto V_h$.

3 Results

3.1 Properties of the TPU materials

TPUs based on methylene diphenyl diisocyanate (MDI), poly (alkylene adipate) and polytetrahydrofuran PTHF® polyols and 1,4-butanediol are most common. Polyethers like PTHF® are less compatible with the MDI based hard chain segments than polyesters and TPUs derived from them show a higher degree of phase separation. The hard domains also tend to be larger and more complex than those found in TPUs based on polyesters. With regard to the short-chain diol, hydroquinone bis(2-hydroxyethylether) (HQEE) yields higher melting hard domains than those produced from 1,4-butane diol.[34] In this paper we investigate MDI-based TPUs from PTHF®, poly (alkylene adipate) and polycaprolactone (PCL) polyols and 1,4-butane diol and HQEE chain extenders. With the present series of polyurethanes the TPU technology field is largely covered. The hard-segment content (HSC) has been kept constant for all TPUs and amounts to 51 wt.-%. In regard to their mechanical properties (see Table 1) the TPUs based on PTHF® (mbt and mqt) are significantly softer (5 – 10 shore-D units) than the polyester based TPUs, which may originate from a higher degree of phase separation. In this respect the use of HQEE or BD has only a minor effect on the polymer hardness (1 – 4 shore-D units). Although being soft, the highest tensile strength at break is measured for mbt. Another observation made is that the HQEE based TPUs show significantly lower values of both weight-average molecular mass M_w and tensile strength at break than those produced from BD. The HQEE based hard chain segments have a higher tendency to phase-separate than those from BD, causing the phase separation to start already at a lower conversion. This earlier phase separation is believed to be the origin of the reduced M_w build-up, and consequentially poorer ultimate tensile properties. Early phase separation may also affect the polymer morphology and the nature of the hard domains. The combined effect of differences in chain topology and polymer mor-

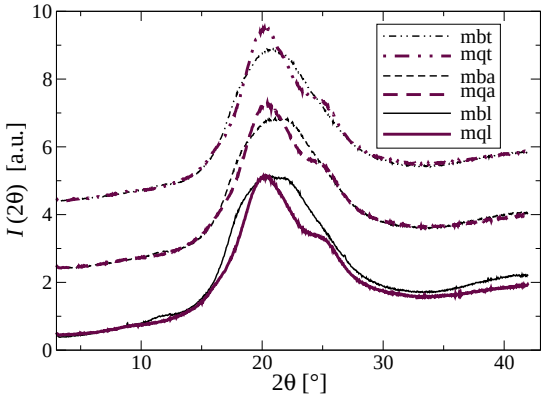

Figure 2: Thermoplastic polyurethane materials hand-cast from different raw components. WAXS scans $I(2\theta)$ (wavelength $\lambda = 0.1542$ nm) of the virgin isotropic materials. Some curves are shifted in vertical direction for clarity

phology may be reflected in the morphologies and their evolution under strain, notably for the polymer mqt.

3.2 WAXS scans

Figure 2 presents the WAXS scans of the studied materials. For mbt and mba only an amorphous halo is observed. All materials with the chain extender HQEE exhibit broad but clear crystalline reflections in addition, and mbl is in between. This shows that the HQEE-based hard domains are more perfectly ordered than those from BD.

WAXS results monitor correlations on the scale of several Ångströms. The strongest scattering effect is related to the contrast between chains and vacuum. Thus some information on the orientation distribution of the normal-direction to the chains may be obtained[35] as a function of strain. Beyond that, even short-range correlations between different chemical groups along the chain may be detectable. On the other hand, the SAXS monitors the two-phase morphology on the scale of nanometers, e.g. the sizes of hard and soft domains and their arrangement in space. For distorted materials of low crystallinity like polyurethanes the morphological relations between both views appear weak, as a previous study has shown[35] and a WAXS study may be reported separately from a SAXS study.

In a tensile test it is expected that the WAXS amorphous halo becomes oriented. It demonstrates the orientation of the normal to the chain direction. For the semicrystalline materials crystalline reflections may orient, grow or decrease during the straining.

From the shape of oriented peaks some information of the orientation distribution of the crystals may be obtained. Similar to the analysis of the orientation of the amorphous halo one does not obtain absolute values, because there is no easy way to determine the background that must be considered.[35] Nevertheless, limits and trends for an uniaxial orientation parameter[22,36] can be determined. Similarly, the variation of the integral intensity of separated crystalline reflections as a function of strain yields indications of strain-induced crystallization or melting. Of course, the integration has to be carried out in 3D reciprocal space and not only in the detector plane.

3.3 The tensile tests

Figure 3 shows the stress-strain curves (true stress vs. local strain) measured during the straining experiments at the synchrotron. Bear in mind that the tensile strength σ_{max} from Table 1 is expressed in engineering stress, $\sigma_{eng} \approx \sigma/(1+\varepsilon)$. The local strain ε is computed from the movement of two fiducial marks close to the point of X-irradiation. This is not the engineering strain which is computed from the movement of the machine cross-heads. Materials become stronger, when the chain extender BD (thin lines) is replaced by HQEE (bold lines). Strengthening correlates with the de-

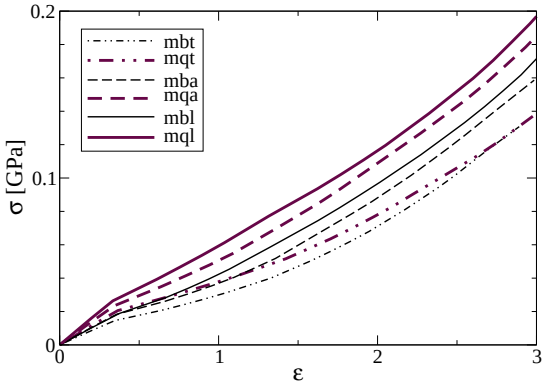

Figure 3: Hand-cast thermoplastic polyurethane materials. True stress σ vs. local strain ε at the position of X-irradiation as measured in situ during the tensile tests

tectability of crystallites (Figure 2).

Related to the soft-segment component the softest material (dashed-dotted) contains PTHF®, the medium one (dashed) is based on adipic ester, and the hardest one (solid line) has soft segments from PCL. This shows that the tensile strength is determined by the chain extender and the employed polyol. The differences in tensile strength could originate from differences in phase separation and intramolecular interactions between the polyol segments. A comparison with the WAXS curves (Figure 2) further indicates a correlation with crystallinity of the hard domains: in the hardest material the crystallites are big enough to be clearly detected.

3.4 SAXS data accumulated during the tests

Figure 4 presents recorded scattering patterns $I(s_{12},s_3)$ and CDFs $z(r_{12},r_3)$ computed from them. In fact, only central cutouts are displayed and only the long-period face $-z(r_{12},r_3) > 0$ of the CDFs is shown. CDFs visualize the local structure in the neighborhood of a domain: Each peak shows, in which

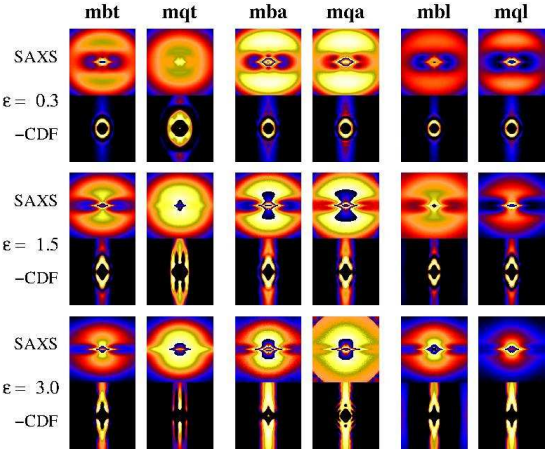

Figure 4: Selected SAXS data from continuous straining experiments of 6 hand-cast TPU materials. ε is the strain. Straining direction is vertical (s_3, r_3 resp.). The top pattern in each line is the scattering intensity ("SAXS"), shown as $\log(\log(I(s_{12},s_3)))$, $-0.15\,\mathrm{nm}^{-1} \leq s_{12},s_3 \leq 0.15\,\mathrm{nm}^{-1}$. The bottom pattern in each line presents the long-period peaks in the chord distribution function ("-CDF"), $-z(r_{12},r_3)$, $-50\,\mathrm{nm} \leq r_{12},r_3 \leq 50$ nm on a logarithmic pseudo-color intensity scale

direction and distance neighbor domains are found. It appears worth to mention that scattering cannot detect the presence of a co-continuous morphology. This is a consequence of the mathematical relation (notably: an autocorrelation) between structure and scattering pattern. Thus in the SAXS data, domains that bend away from the normal plane to the straining direction appear as if they were cut-off in the direction transverse to the straining (cf. the discussion of the breadth of the long-period peaks below).

For each material a row of images is presented. The leftmost row shows the softest material, the hardest one is found on the right. In each row the strain ε increases from top to bottom. Compared to respective machine-cast materials[9] the SAXS patterns look similar, but the CDFs are fundamentally different. With the hand-cast materials the long-period peaks are broad (in vertical direction). They are neither narrow nor found in static discrete bands like with the machine-prepared TPUs. Instead, the CDFs look very similar to those from a previous TPU study of some of us.[37] Also those samples were prepared by the hand casting process.

3.5 Nanostructure from CDF analysis

The 6 materials exhibit morphological differences. Compared to the given overview they are more clearly presented in meridional cuts of the CDFs (Figure 5). In one of the subfigures straight lines are drawn as guides to the eye. They connect the first-order peaks (solid) and the second-order peaks (dashed). In each strip the brightest spot on the central line indicates the most-frequent long period.

Only mqt shows peculiarities that have previously been found with machine-cast materials.[9] It is the softest-but-one material (Figure 3). The hard domains of the softest material are fortified by the chain extender HQEE. Up to $\varepsilon \approx 1$ several long-period peaks are observed. This is similar to the morphology found in machine-cast materials,[9] but here no static long-period bands are observed. Thus the series of peaks only indicates morphological disintegration[37,38] of hard domains, but the extensibility of these morphological entities is not limited as is the case with the mentioned machine-cast materials.

Straining divides the hard domains into different classes. The brightest spot (most frequent class) has the shortest long period. After an initial upward movement at low strain, the spot moves down as the strain increases further. This means relaxation after initial increase. Simultaneously a long tail emerges which points upward. This means that the distribution of long periods becomes extremely broad and asymmetric. The other classes of hard domains have disappeared. It seems that they have been weaker than the domains from the most frequent class.

The discussed tail formation is found with all materials. It has earlier been observed with other hand-cast polyurethanes.[37] Both a long-period relaxation and a formation of a long tail have been explained by a "sacrifice-and-relief" mechanism[37] that requires the destruction of a considerable amount of hard domains.

To capture the nanostructure change quantitatively by means of the long period peak, we track its position and shape during the tensile tests. In previous work on polyurethanes we have done this as well.[9,37,39] Figure 6 presents the evolution of the nanoscopic strain $\varepsilon_n(\varepsilon)$ computed from the most-frequent long period. Only the material mqt exhibits the relaxation behavior known from machine-cast materials[9] that has already been discussed qualitatively. With the other hand-cast materials the known[9] slow increase of the nanoscopic strain $\varepsilon_n(\varepsilon) \approx 0.6\,\varepsilon$ continues up to the end of the experiment. We explain the low slope ($0.6 < 1$) by the rigid-

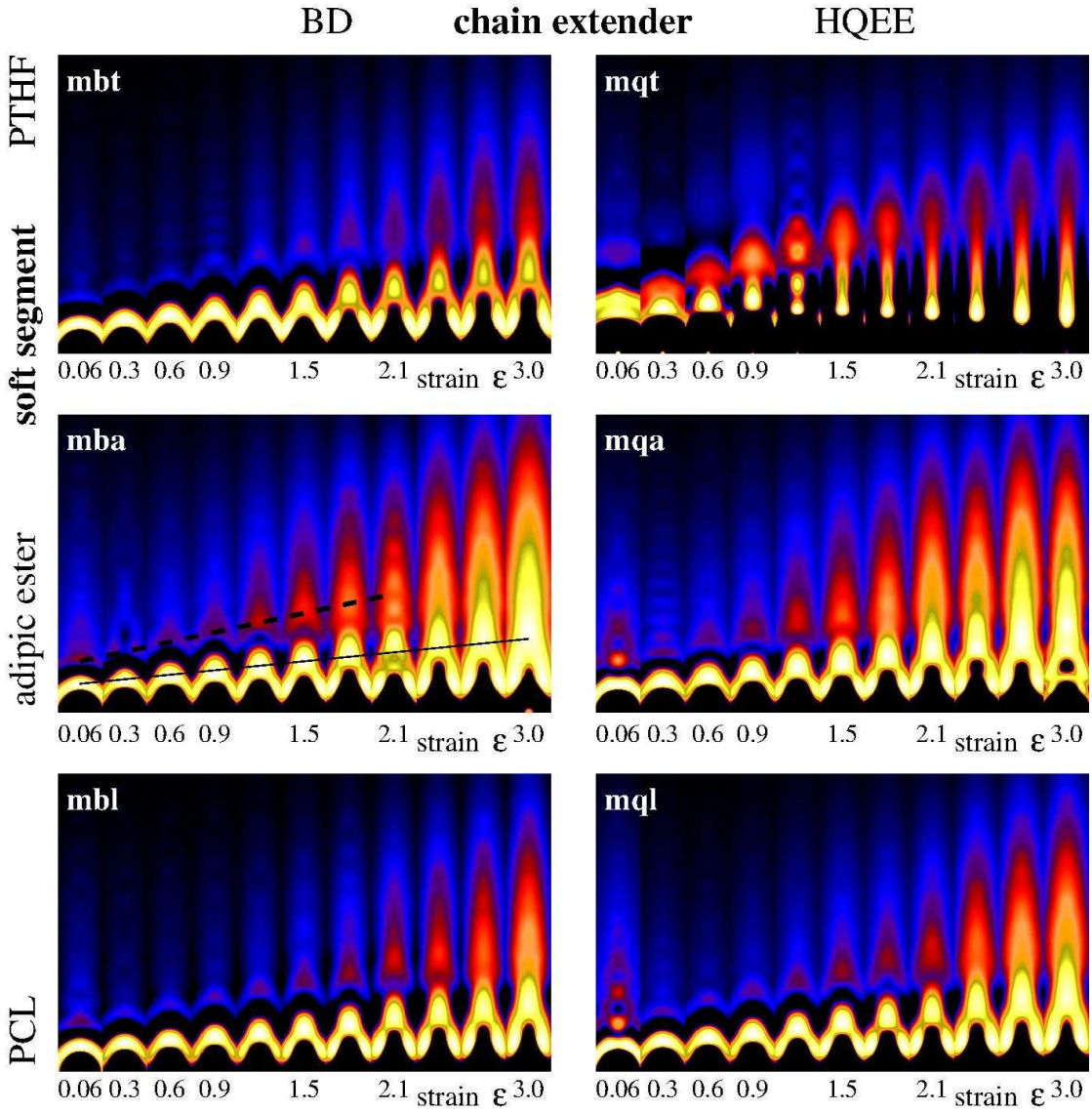

Figure 5: Meridional long-period regions cut from the CDFs. $-z(r_{12,}r_3)$ $0 \leq r_3 \leq 50\,\mathrm{nm}$, $|r_{12}| \leq 8$ nm is presented on a varying $\log(\log(-z))$ intensity scale In subfigure mba: Lines indicate first-order (solid) and second-order (broken) long period peaks

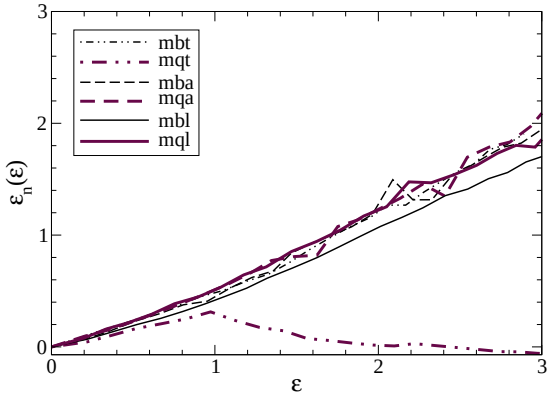

Figure 6: Nanoscopic strain $\varepsilon_n(\varepsilon) = r_{3,Lmax}(\varepsilon)/\varepsilon$ computed from the position $r_{3,Lmax}(\varepsilon)$ of the first-order long period maximum in the the CDF as a function of the macroscopic local strain ε

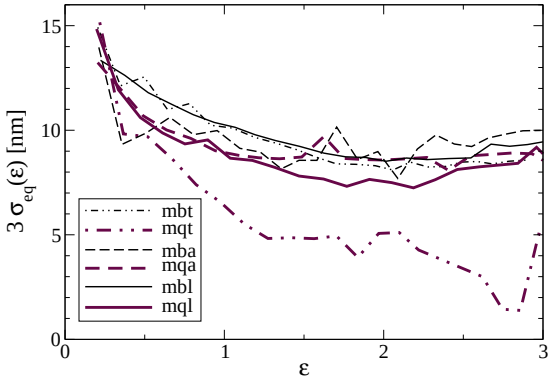

Figure 7: $\sigma_{eq}(\varepsilon)$ computed for the evolution of the first-order long period peak is a measure of the transverse straight extension of the hard domains

ity of the hard domain (average height: $\overline{H}_h$) that is part of the long period $\overline{L} = \overline{H}_h + \overline{H}_s$.

The breadth of the long-period peak yields a measure of some average straight hard-domain extension transverse to the straining direction. By "straight extension" we indicate that the anisotropic SAXS cannot determine, if the loss of correlation is a consequence of either narrow hard-domains or of laterally extended hard-domains which bend away from the transverse plane after a short distance. Sufficient anisotropy of the CDF is required for its determination. Figure 7 displays the results. The hard domain extensions decrease with increasing strain. This indicates disruption. Most of the materials show a very similar behavior with an almost constant value reached for $\varepsilon > 1.5$. There the disruption appears to have stopped.

Again, an exception is the material mqt. It appears logical that a material with different classes of hard domains shows a more complex decay curve than the other materials, but we have no explanation for the observation that in the interval $1 < \varepsilon < 2$ the stable hard domains are much narrower than with the other materials. This feature can only be elucidated by dedicated experiments. We speculate that the origin of the observed phenomena could lie in the preparation of the sample and its premature phase separation.

3.6 Bonart's longitudinal scattering

Direct analysis. The longitudinal scattering $\{I\}_1(s_3)$ exhibits morphological differences, as well. Figure 8 displays the results. A first inspection of the data shows that the PTHF® based TPUs show a more intense scattering profile than those based on the polyesters. This is readily explained by different polarity. Because PTHF® is less polar than the two polyesters, a stronger phase separation should have occurred, resulting in a more intense scattering.[34]

In the PTHF® based materials (Figure 8 upper subfigures) substitution of the chain extender BD by HQEE has several effects. The intensity is doubled, the peak position is affected, and its response to strain is changed. With the peculiar material mqt the long-period peak is much less pronounced than with the material mbt. This is readily explained by the observed superposition of several hard domain classes.

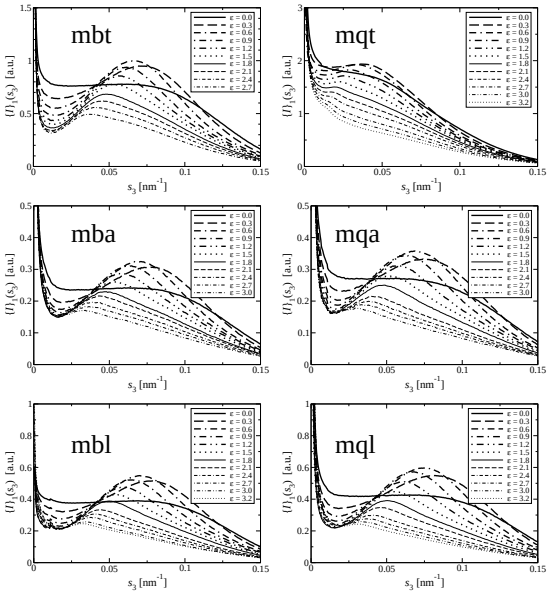

Figure 8: Evolution of Bonart's longitudinal scattering as a function of strain. Intensities are normalized for constant X-ray flux and constant irradiated volume

Such strong effects are not found with the middle and the bottom subfigures, but minor differences with respect to both the varying long-period and changing intensity can still be read from the curves. In Figure 8 the area under the curves is the scattering power Q. Curves $Q(\varepsilon)$ are reported in Figure 9. Obviously, the chain extender BD yields lower Q than HQEE. The relative variations of Q as a function of ε are similar for all materials. If the initial volume fraction of hard domains $v_h(\varepsilon = 0) < 0.3$, a decrease of Q is approximately proportional to a reduction of v_h. For all materials an initial increase is followed by a decrease. This qualitative result concerning v_h can be quantified for the studied samples with moderate effort, because the morphology of the hand-cast materials is blurred considerably. For this purpose the corresponding interface distribution functions are analyzed.

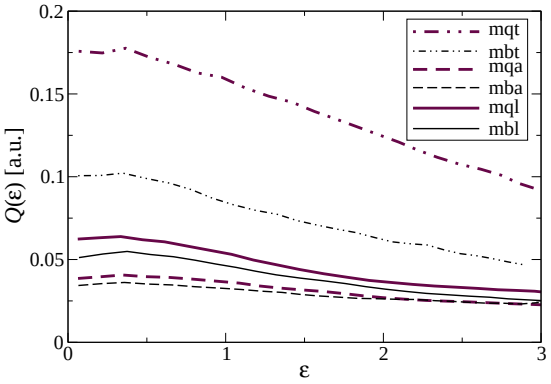

Figure 9: Variation of the scattering power Q in the tensile tests

IDF analysis. From Bonart's longitudinal scattering $\{I\}_1(s_3)$ and interface distribution function $g_1(r_3)$ can always be computed. It describes the statistics and arrangement of domain heights in straining direction r_3. Nevertheless, an analysis that may yield deeper insight is only possible, if the IDF can be fitted by a suitable model. In the case of machine-processed materials[9] a peculiar band structure has been found. This complex topology requires either the construction of an involved morphological model based on quasi-periodicity or the development of appropriate approximations. The inspection of Figure 4 indicates that here an IDF analysis by a simple model appears promising.

In a first step the IDFs are computed and visually inspected. Their features and the trend as a function of ε is similar for all materials. Figure 10 shows 3 IDFs of the material mql at different strains. There is a very strong positive peak which contains the thickness distributions of hard and soft domains, $H_h(r_3)$ and $H_s(r_3)$, respectively. The first negative peak is the long period distribution $L(r_3)$. It is extremely broad and shallow. This means that one of the positive distributions ($H_h(r_3)$ or $H_s(r_3)$) must as well be broad and shallow. We assume that this is the distribution of soft domains, $H_s(r_3)$.

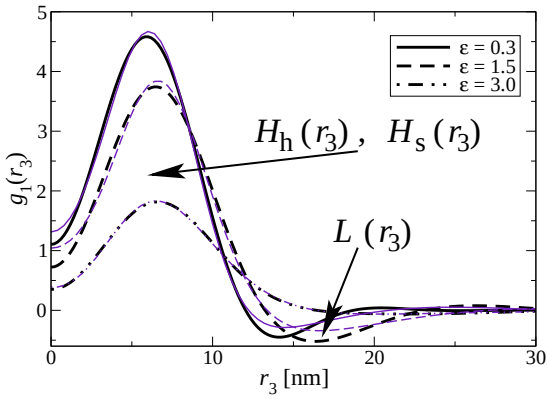

Figure 10: Material mql. Interface distribution functions (IDF) $g_1(r_3)$ computed from $\{I\}_1(s_3)$ for selected ε. The data of the other materials look similar. Bold lines: measured data. Thin lines: fits by the stacking model. The main peak is made from $H_h(r_3)$ and $H_s(r_3)$, the height distributions of hard and soft domains in straining direction r_3. Long period distributions $L(r_3)$ are peaking in negative direction

So the very strong positive peak is a good approximation of $H_h(r_3)$, and the rest of the IDF describes the poor correlations among the domains. In other words, the predominant information content of the IDF is particle scattering. In this notion the integral W of the IDF is proportional to the volume of the particles with the narrow height distribution, i.e. to the volume of hard domains. Then in Figure 10 the decrease of the integral with increasing strain describes the loss of hard-domains during the tensile test.

It appears worth to mention that even the uncorrelated particles (from the diffuse particle scattering) contribute to the first peak in the IDF, but only to this peak. The higher peaks beginning with the long-period peak require order among particles. With respect to our tensile experiments we have named such ordered entities “strain probes”.

The shape of the curves indicates that they can be fitted by Gaussian distributions. The blurred morphology of the hand-cast material is demonstrated by the fact that the oscillations in $g_1(r_3)$ have already died out for $r_3 > 25\,\mathrm{nm}$. A short-range model appears to be applicable, and we must be careful to choose a simple model with few parameters because the few broad peaks overlap considerably.

The strong positive domain peak dominates the IDF. Even if second-order features are not correctly considered by a simple model, it may be able to separate the hard-domain peak $H_h(r_3)$ from the contribution of the discrete scattering. A failure of the separation can be assessed by discussing the plausibility of the extracted morphological parameters as a function of ε.

Thin lines in Figure 10 show the best fits using the one-dimensional stacking model.[26,31] The strong peak appears to be fitted well, but the long-period peak $L(r_3)$ is poorly fitted for low and medium strain. This shortcoming may be related to remnant features of quasi-periodic sequences of hard and soft segments that have been found with machine-cast TPUs.[9]

Results of the fits by nonlinear regression[30] of $g_1(r_3)$ are presented in the following figures. They present morphological parameters as a function of strain.

Figure 11 displays the variation of the average hard-domain height $\overline{H}_h(\varepsilon)$ for all materials. $\overline{H}_h(\varepsilon)$ varies only slightly with ε and has a value of about 8 nm. 8 nm is also the height of hard domains that has been extracted from the data of machine-cast materials[9,40] containing MDI hard segments, as well. $\overline{H}_h$ has been identified from a peculiar quasi-periodic signature of the CDF peaks and related to a sequence of 2 MDI segments along the chain of the copolymer. This is in excellent agreement with crystallographic data[41–43] from model urethanes made from alternating MDI and BD. The papers find unit cell heights of 3.8 nm. Thus a hard block that contains 2 MDI

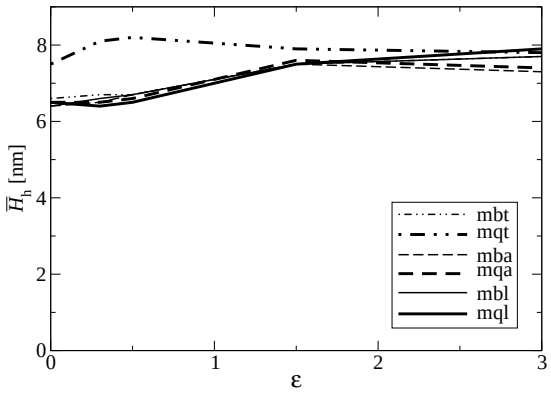

Figure 11: Variation of the average hard domain height, $\overline{H}_h(\varepsilon)$ as determined from fits of $g_1(r_3)$

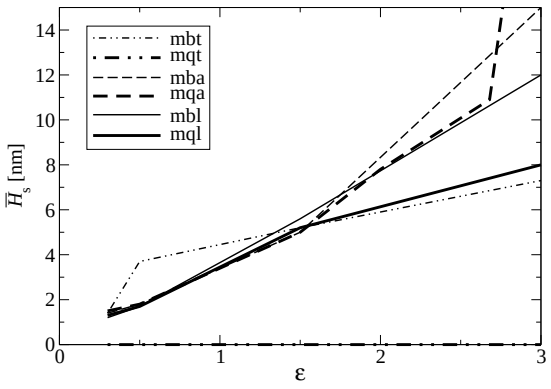

Figure 12: Average soft domain height, $\overline{H}_s(\varepsilon)$ of the studied materials as determined from fits of $g_1(r_3)$

segments should have a height of 2×3.8 nm = 7.6 nm.

Also the relative breadths $\sigma_h/\overline{H}_h$ of $H_h(\varepsilon)$ vary only slightly between 0.4 and 0.6. Thus, the hard domain ensemble has an almost constant average height and distribution width. Inelastic behavior is what one expects. This finding indicates that $H_h(\varepsilon)$ has probably been separated from the scattering data successfully.

There are slight changes that may be related to growth and destruction of hard domains. Thickness growth at low strain is only observed for the material mqt. There the other materials exhibit constant thickness followed by increasing average thickness for $0.5 < \varepsilon < 1.5$. We will show that this is already the region in which hard domains are destroyed. So the finding shows that for most of the materials thin hard domains fail more easily than thick ones.

Figure 12 presents $\overline{H}_s(\varepsilon)$, the variation of the average soft-domain height between two hard-domains. To keep the effort manageable only some of the measured data have been processed. The strong and monotonous increase of $\overline{H}_s(\varepsilon)$ describes the expected contribution of the soft phase to the nanoscopic elongation of the materials. Only for the material mqt $\overline{H}_s(\varepsilon)$ iterates towards zero. There the distributions $H_s(r_3)$ are extremely wide. The simple model is unable to fit the different morphological classes (see above). The observed monotonous increase of the average soft domain height is a second indication for a successful separation of the distributions $H_h(r_3)$.

The parameters of $H_s(r_3)$ must not be discussed in detail. In particular its width compensates the systematic deviations of the morphology from the simple stacking model. A straight solution would be to use a two-component model. Then an additional component would describe the uncorrelated hard domains only. Nevertheless, in this case cross-correlation among the parameters of the two models returns morphological parameters of low significance. The reason is the poorly structured scattering pattern of the polyurethanes.

Figure 13 shows the result of the weight analysis (cf. derivation of Eq. (4)). For all materials a strain-induced formation of hard domains is observed up to $\varepsilon \approx 0.5$.

Moreland and Wilkes[44] have identified a two-step orientation–elongation mechanism. The region $\varepsilon < 0.5$ has been associated with low hysteresis. Here the hard domains aligned

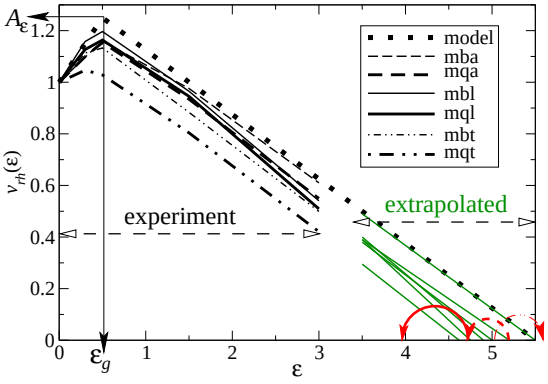

Figure 13: Variation of the relative volume fraction of hard domains, $v_{rh}(\varepsilon)$ for $0 \leq \varepsilon \leq 3$ as determined from $\overline{H}_h W(\varepsilon)$ in fits of $g_1(r_3)$. Characteristic parameters A_ε and ε_g are indicated with the model curve (dotted). Linear extrapolations hit the ε-axis at a model strain-at-break, ε_{bm}. Circular arrows point at ε_b values from Table 1, if significant differences are observed

more or less reversibly in the strain direction. For $\varepsilon > 0.5$ hard domains are disrupted by pulling away individual segments from the hard domains. Our investigation supports and further refines this mechanism. In analogy to the accepted mechanism of strain-induced crystallization, we imagine that the chain orientation induced by a low tensile force induces an additional separation of the phases.

The gain is different for the different materials. It is lowest for mqt and highest for mbl. For $0.5 < \varepsilon < 3$ all materials show a linear decrease of the hard-phase volume. In several previous studies we have found by different analysis methods that hard domains must be sacrificed. Our trial plot indicates that a simple quantitative relation appears to hold for all the investigated materials.

As sketched in Figure 13 we define two material constants. A_ε is a tensile augmentation (in analogy to the definition of the tensile strength in a stress-strain curve), and ε_g is the corresponding end-of-growth strain, i.e. $A_\varepsilon = v_{rh}(\varepsilon_g)$. The slope of the subsequent destruction decay, $c_{r\varepsilon} = dv_{rh}/d\varepsilon = 0.25$ is identical for all materials. It defines the relative tensile hard-domain consumption. A reason for the identical value may be that all materials share the same HSC. Comparing the variety of chemical compositions, the identical hard-domain consumption per strain-step show that this is a principle which appears to govern the straining of several important classes of TPU. This should be different for, e.g., chemically crosslinked materials.

In summary, for the studied materials a first-approximation model for the relative volume change of hard domains is

$$v_{rh}(\varepsilon) \approx \begin{cases} 1 + (A_\varepsilon - 1)\,\varepsilon/\varepsilon_g & \text{for } \varepsilon \leq \varepsilon_g \\ A_\varepsilon - c_{r\varepsilon}\,(\varepsilon - \varepsilon_g) & \text{for } \varepsilon > \varepsilon_g \end{cases} . \tag{5}$$

Does the material break, if almost all hard domains are consumed? This would mean $v_{rh}(\varepsilon_b) = 0$, and if the linear relation of Eq. (5) holds up to the materials failure, then the approximation

$$\varepsilon_b \approx A_\varepsilon / c_{r\varepsilon} + \varepsilon_g \tag{6}$$

should be valid. Comparison with Table 1 and the extrapolations sketched in Figure 13 indicates that Eq. (6) is not too bad, in particular considering the wide variation in chemical composition of the TPUs. The differences may be related to secondary mechanisms like fracture, strain-induced crystallization of the soft phase and subtle differences in chain topology and polymer morphology.

For the materials with HQEE but not PTHF®, ε_b is somewhat shorter than predicted, for the inverse composition (BD and PTHF®) ε_b is longer. This indicates that secondary mechanisms which cause deviations from the typical cohesion of a TPU may probably be tailored by choice of its components and processing conditions.

4 Conclusions

The studied hand-cast TPU materials exhibit a morphology in which particles (hard domains) are almost placed at random, and the present faint correlations do not reach far. Therefore, one can describe the topology of their domains by a simple standard two-phase model, fit the data with low error and thus quantitatively track the evolution of the morphology in the strain test. As has been derived in the data evaluation section, the product of two fit parameters is proportional to the volume of the dilute phase. For the studied materials the dilute phase is formed by the hard domains, as has been verified by comparing the height distributions of soft and hard domains.

For all materials similar curves describe the variation of the hard-domain volume as a function of strain. For $\varepsilon > 0.5$ the volume decreases linearly and the material breaks, when all domains are destroyed. This correlation with the macroscopic mechanical parameter ε_b indicates how fundamental the destruction of physical crosslinks (the hard domains) appears to be with the non-crosslinked polyurethanes.

As an explanation for the poorly modulated discrete scattering of hand-molded materials, we have adopted a double-sequence variability of the hard and soft blocks along the chains. The second variability can be generated by factors that are related in the broad sense to the processing and intrinsic properties of these materials. We have referred in detail to the incomplete mixing, but there are also other factors that are governed by the kinetics and thermodynamics of the phase separation process. Despite the wide choice in raw materials and the basic preparation technique that have been used to produce the TPUs, they all have shown a common behavior which is captured in Eq. (5) and Eq. (6).

In order to be able manage the experimental and evaluation effort of a SAXS study we have varied the TPU composition, but have kept constant the hard-segment content. Therefore we have been able to show that the found empirical relation is valid for a broad range of compositions, but we have not been able to determine, if the tensile domain consumption $c_{r\varepsilon}$ is a function of HSC. Finally, we hope that Eq. (5) and Eq. (6) may become useful in the modeling of material properties of thermoplastic polyurethanes.

Acknowledgements. The authors thank the Hamburg Synchrotron Radiation Laboratory (HASYLAB) for beam time granted in the frame of project I-2011-0087. Almut Barck is acknowledged for the WAXS scans and Benjamin Nörnberg for tensile tests.

References

[1] Petrović, Z. S.; Ferguson, J., *Progr. Polym. Sci.* **1991**, 16, 695–836.

[2] Axelrood, S. L.; Hamilton, C. W.; Frisch, K. C., *Ind. Eng. Chem.* **1961**, 53, 889–894.

[3] Clemitson, I. R., *Polyurethane Casting Primer*, CRC Press, Boca Raton, FL, **2012**.

[4] Harpen, F.; Luinstra, G. A.; Eling, B., in Moritz, H.-U., ed., *11th Int. Workshop on Polymer Reaction Engineering. Book of Abstracts*, Dechema e.V., Frankfurt, **2013** p. 135, p. 135, poster P68.

[5] Rausch Jr, K. W.; Sayigh, A. A. R., *Ind. Eng. Chem. Prod. Res. Development,* **1965**, 4, 92–98.

[6] Yen, M.-S.; Kuo, S.-C., *J. Appl. Polym. Sci.* **1996**, 61, 1639–1647.

[7] Fan, L. H.; Hu, C. P.; Ying, S. K., *Polym. Eng. Sci.* **1997**, 37, 338–345.

[8] Bell, J. P., *J. Appl. Polym. Sci.* **1982**, 27, 3503–3511.

[9] Stribeck, A.; Jokari Sheshdeh, F.; Pöselt,

E.; Eling, B.; in't Veld, P. J.; Goerigk, G. J.; Hoell, A., *J. Polym. Sci. Polym. Phys.* **2015**, 53, 1213–1223.

[10] Stribeck, N., *J. Polym. Sci., Part B: Polym. Phys.* **1999**, 37, 975–981.

[11] Speckhard, T. A.; Cooper, S. L., *Rubber Chem. Technol.* **1986**, 59, 405–431.

[12] Auffarth, S.; Boudou, M.; Eling, B.; Reese, O., *Siliciumdioxid-Dispersionen*, Patent, WO2012032099 A1, **2012**, March 15. See example D1.

[13] Bonart, R., *J. Macromol. Sci. Part B: Physics* **1968**, 2, 115–138.

[14] Li, Y.; Gao, T.; Chu, B., *Macromolecules* **1992**, 25, 1737–1742.

[15] Hu, W.; Koberstein, J. T., *J. Polym. Sci. Part B: Polym. Phys.* **1994**, 32, 437–446.

[16] Martin, D. J.; Meijs, G. F.; Gunatillake, P. A.; Mccarthy, S. J.; Renwick, G. M., *J. Appl. Polym. Sci.* **1997**, 64, 803–817.

[17] Galambos, A. F., *The effect of hard-segment content, temperature, and thermal history on the morphology of polyurethane block copolymers*, Ph.D. thesis, Dept. Chem. Eng., Princeton University, **1989**.

[18] Yilgör, E.; Yilgör, I.; Yurtsever, E., *Polymer* **2002**, 43, 6551–6559.

[19] Pichon, P. G.; David, L.; Méchin, F.; Sautereau, H., *Macromolecules* **2010**, 43, 1888–1900.

[20] Stribeck, N.; Nöchel, U.; Funari, S. S.; Schubert, T., *J. Polym. Sci. Polym. Phys.* **2008**, 46, 721–726.

[21] Stribeck, N., in Karger-Kocsis, J.; Fakirov, S., eds., *Nano- and Micromechanics of Polymer Blends and Composites*, vol. 1, Hanser Publisher, Munich, **2009** pp. 269–300, pp. 269–300.

[22] Stribeck, N., *X-Ray Scattering of Soft Matter*, Springer, Heidelberg, New York, **2007**.

[23] VNI, *PV-WAVE manuals*, V 7.5, Houston, TX, USA, **2007**.

[24] Bonart, R., *Kolloid Z. u. Z. Polymere* **1966**, 211, 14–33.

[25] Ruland, W., *Colloid Polym. Sci.* **1977**, 255, 417–427.

[26] Stribeck, N., *ACS Symp. Ser.* **2000**, 739, 41–56.

[27] Ruland, W., *J. Appl. Cryst.* **1971**, 4, 70–73.

[28] Vonk, C. G., *J. Appl. Cryst.* **1973**, 6, 81–86.

[29] Rathje, J.; Ruland, W., *Colloid Polym. Sci.* **1976**, 254, 358–370.

[30] Stribeck, N., *Colloid Polym. Sci.* **2002**, 280, 254–259.

[31] Hermans, J. J., *Rec. Trav. Chim. Pays-Bas* **1944**, 63, 211–218.

[32] Stribeck, N., *Colloid Polym. Sci.* **1993**, 271, 1007–1023.

[33] Stribeck, N., *J. Phys. IV* **1993**, 3, 507–510.

[34] Mackey, P., in Randall, D.; Lee, S., eds., *The Polyurethanes Book*, John Wiley, New York, **2003** pp. 285–294, pp. 285–294.

[35] Stribeck, N.; Zeinolebadi, A.; Ganjaee Sari, M.; Frick, A.; Mikoszek, M.; Botta, S., *Macromol. Chem. Phys.* **2011**, 212, 2234–2248.

[36] Hermans, J. J.; Hermans, P. H.; Vermaas, D.; Weidinger, A., *Rec. Trav. Chim. Pays-Bas* **1946**, 65, 427–447.

[37] Stribeck, N.; Zeinolebadi, A.; Harpen, F.; Luinstra, G. A.; Eling, B.; Botta, S., *Macromolecules* **2013**, 46, 4041–4052.

[38] Kimura, I.; Ishihara, H.; Ono, H.; Yoshihara, N.; Nomura, S.; Kawai, H., *Macromolecules* **1974**, 7, 355–363.

[39] Stribeck, N.; Li, X.; Kogut, I.; Moritz, H.-U.; Eling, B.; Goerigk, G. J.; Hoell, A., *Macromol. Mater. Eng.* **2015**, 300, 699–711.

[40] Stribeck, N.; Li, X.; Eling, B.; Pöselt, E.; in 't Veld, P. J., *J. Appl. Cryst.* **2015**, 48, 313–317.

[41] Blackwell, J.; Lee, C. D., *J. Polym. Sci. Part B: Polym. Phys.* **1984**, 22, 759–772.
[42] Born, L.; Crone, J.; Hespe, H.; Müller, E. H.; Wolf, K. J., *J. Polym. Sci. Part B: Polym. Phys.* **1984**, 22, 163–173.
[43] Christenson, C. P.; Harthcock, M. A.; Meadows, M. D.; Spell, H. L.; Howard, W. L.; Creswick, M. W.; Guerra, R. E.; Turner, R. B., *J. Polym. Sci. Part B: Polym. Phys.* **1986**, 24, 1401–1439.
[44] Moreland, J. C.; Wilkes, G. L.; Turner, R. B., *J. Appl. Polym. Sci.* **1991**, 43, 801–815.